9-8-2005

Imaging solar neutrons below 10 MeV in the inner heliosphere

U Bravar

Recommended Citation

Ulisse Bravar ; Paul J. Bruillard ; Erwin O. Flueckiger ; Alec L. MacKinnon ; John R. Macri ; Procheta C. Mallik ; Mark L. McConnell ; Michael R. Moser and James M. Ryan "Imaging solar neutrons below 10 MeV in the inner heliosphere", Proc. SPIE 5901, Solar Physics and Space Weather Instrumentation, 59010I (September 08, 2005); doi:10.1117/12.617392; http://dx.doi.org/10.1117/12.617392

Imaging solar neutrons below 10 MeV in the inner heliosphere

Ulisse Bravar*[a], Paul J. Bruillard[a], Erwin O. Flückiger[b], Alec L. MacKinnon[c], John R. Macri[a], Procheta C. Mallik[a], Mark L. McConnell[a], Michael R. Moser[b], James M. Ryan[a]
[a]Space Science Center, University of New Hampshire, 39 College Road, Durham, NH 03824, USA
[b]Physikalisches Institut, University of Bern, Sidlerstrasse 5, CH-3012 Bern, Switzerland
[c]Dept. of Physics & Astronomy, Univ. of Glasgow, Kelvin Bldg., Glasgow G12 8QQ, Scotland

ABSTRACT

Inner heliosphere probing of the Sun can be conducted with the proposed Solar Sentinel spacecraft and mission. One of the key measurements that can be made inside the orbit of the Earth is that of lower energy neutrons that arise in flares from nuclear reactions. Solar flare neutrons below 10 MeV suffer heavy decay losses before reaching 1 AU. For heliocentric radii as close as 0.3 AU, the number of surviving neutrons from a solar event is dramatically greater. Neutrons in the energy range 1-10 MeV provide a new measure of heavy ion interactions at low energies, where the vast majority of energetic ions reside. An instrument to make these measurements must be compact, lightweight and efficient. We describe our progress in developing a low-energy neutron telescope that can operate and measure neutrons in the inner heliosphere and take a brief look at other possible applications for this detector.

Keywords: neutrons, solar flares, remote particle sensing

1. INTRODUCTION

Solar neutron measurements can provide key information on energetic processes that occur at the Sun, such as the acceleration of charged particles in solar flares. By combining these measurements with γ-ray and Earth-based cosmic-ray observations, it becomes possible to reconstruct the entire energy spectrum of solar protons and ions from a few MeV up to GeV energies[1].

Since low energy solar neutrons do not survive in significant numbers by the time they reach the Earth, the energy range below ~20 MeV is hardly accessible at 1 astronomical unit (AU). As an example, a solar neutron with kinetic energy E_{kin} = 10 MeV and a mean lifetime τ = 887 s reaches on average a distance of 0.13 AU from the Sun prior to decaying. About 30% of these particles travel to 0.3 AU and only 2% get to 1 AU. Therefore, in order to observe low energy solar neutrons, one has to operate optimized neutron spectrometers on missions to the innermost heliosphere. Considering that the need to measure neutrons below 10 MeV is recognized by NASA as a solar physics objective, solar neutron detectors are ideal candidates for the NASA Solar Sentinels[2] project, presently under review by a Science Definition Team. In particular, the planned L_1 constellation of Inner Heliospheric Sentinels provides the perfect platform for such detectors. The most inner spacecraft, orbiting the Sun at 0.3 AU, may be outfitted with neutron spectrometers that are sensitive to neutrons from a few MeV up to ~100 MeV, while those at larger radii may be equipped with spectrometers that are optimized for higher energies.

This paper describes the *Fast Neutron Imaging Telescope* (FNIT)[3], a detector that is being developed by an international team primarily to measure solar neutrons in the energy range 2-20 MeV with capabilities above that range too. The range 20-250 MeV could be covered by a separate instrument, the *SOlar Neutron TRACking imaging spectrometer* (SONTRAC)[4], engineered by the same team with the addition of University of Alabama - Huntsville. The development of fast neutron detectors will also benefit several national needs, including those of interest to the Department of Energy, the National Nuclear Security Administration, and the Proliferation Deterrence Program within the Office for Nonproliferation and National Security. Some of these application needs include special nuclear material (SNM) detection, SNM search, SNM characterization and nuclear waste detection and monitoring.

* Ulisse.Bravar@unh.edu; phone 1 (603) 862-3868; fax 1 (603) 862-3584

Solar Physics and Space Weather Instrumentation, edited by Silvano Fineschi, Rodney A. Viereck,
Proc. of SPIE Vol. 5901, 59010I, (2005) · 0277-786X/05/$15 · doi: 10.1117/12.617392

2. NEUTRON SOURCES

2.1 Solar neutrons

Understanding the acceleration of both solar electrons and ions to high energies is an important step in solving the solar flare problem. Although substantial observational and theoretical progress have been made during the last two solar cycles, gaining a complete understanding of the acceleration and transport mechanisms for protons and/or ions remains one of the key goals of solar physics research[5,6]. Some of the nagging problems are:

- the rapid acceleration of high-energy electrons and protons (up to several hundred MeV) on time scales of ~1 s;
- GeV proton acceleration on time scales of < 1 minute;
- the acceleration of GeV protons for periods of over 10 hours;
- the nature of the delay of the γ-ray line emission with respect to the emission in hard X-rays;
- the variability of the ion spectrum in shape and composition over the course of a flare; and
- how ions possess a major fraction of the flare energy during the impulsive phase.

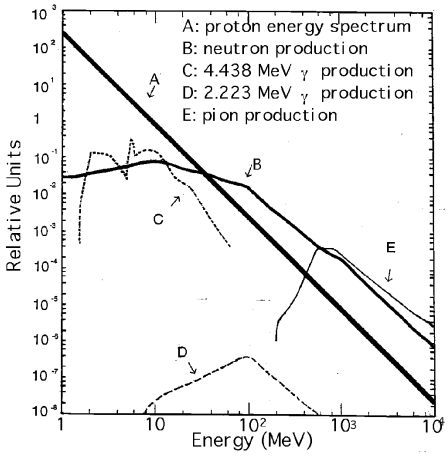

Figure 1. Schematic representation of solar neutron and γ-ray production[1].

To address these questions a better knowledge of the accelerated ion spectrum and composition are necessary. Although solar flare protons and ions are likely being detected in space in "impulsive" particle events, the closest we can come to an unbiased measure of the energetic proton spectrum at the flare site comes from the secondary neutral radiation, *i.e.* γ-rays and neutrons, the parent of which is the accelerated proton spectrum at the flare site.

Nuclear γ-rays, neutrons and γ-rays associated with pions each provide important information about different parts of the proton spectrum at the flare site. Figure 1 illustrates how different particle and photon species measurements are necessary to sample or measure the full energetic-proton population. With the spectrum determined at the low end by way of γ-ray line ratios and at the high end by way of π-related emission, one must question the need to measure anything else. Over the last two solar cycles we have witnessed a range of energetic flares, some exhibiting γ-ray emission above 50 MeV, but most not. Those that do not exhibit such emission yield no direct information on the ion spectrum above ~40 MeV/nuc. For these events, we must rely on neutrons to provide that information. An excellent means of determining the 40-300 MeV proton spectrum is via direct measurement of neutrons. For a small number of events, this was done with the COMPTEL, OSSE and EGRET instruments aboard the Compton Gamma Ray Observatory (CGRO)[7]. By carefully examining the neutron emission in the inner heliosphere and comparing that to the corresponding γ-ray spectrum, one can deduce not only the intensity of the ion spectrum at low energies but also its composition in terms of richness of ions with A>1.

When making neutron measurements, it is important to not only measure the neutron energy, but also to record the arrival time of the individual neutron to compute the origination time at the Sun. This allows one to study the evolution of the spectrum shape and its composition as the flare progresses. There is ample evidence that significant changes in the spectrum and ion composition occur over the course of a complex event.

2.2 Special nuclear material

One of the critical gaps in national security is the inability to efficiently detect and identify SNM. These materials—specifically uranium and transuranics—emit neutrons via spontaneous or induced fission. Unlike the other forms of radiation produced by SNM samples (*e.g.* γ-rays), copious and penetrating neutron emission with a bulk energy of the order of the MeV is unique to fissionable material. Neutron detection, therefore, is of particular importance for SNM detection for security and proliferation deterrence. While improvements in all forms of radiation detection are necessary to close this gap, there are unique problems in neutron detection, imaging and energy measurement.

Current neutron detectors used in SNM surveys do not directly detect the fission neutrons, but rather register their presence only after moderation, *i.e.* after they have lost all original energy and directional information. Because of this

limitation, current detection systems often do not have sufficient sensitivity to detect problematic and dangerous amounts of fissionable material. For example, one pound of ^{239}Pu can produce little more than background-level neutron fluxes at a distance of only several meters. At present, this makes searching for clandestine amounts of SNM a major shortcoming in nuclear security systems. Sensitivities one to two orders of magnitude better are necessary to make a significant improvement to this situation.

3. NEUTRON DETECTION

3.1 Methodology

Because they are electrically neutral, neutrons must be detected using indirect means. The FNIT design, in its full configuration, is composed of multiple layers of position-sensitive organic scintillator detectors operating in coincidence detection mode. For each detected incident neutron, the instrument measures the locations, relative time and energy deposits of all resultant n-p interactions. These data are analyzed on an event-by-event basis using the equations of n-p scattering kinematics to determine each neutron's energy and angle of incidence.

At MeV energies the n-p scattering cross section is large. The recoil proton from an n-p scatter is a highly ionizing particle and is easily detected with a suitable instrument. For instance, in a plain scintillator plate, light produced by the proton-ionization energy loss can be measured with appropriate optoelectronics (*e.g.* photomultiplier tubes) and its intensity related to the kinetic energy of the scattered proton. This type of detector has a number of desirable features. It is compact, lightweight, fast and simple. In its basic form, however, it is omni-directional, and therefore cannot achieve the levels of sensitivity required for neutron source characterization. A directional, or better still, an imaging detector can be far more selective and discriminating against background, yielding much improved sensitivity. To perform neutron imaging, one must follow the path of the neutron, measuring the location and energy deposits of each n-p interaction.

Consider the case shown in Figure 2. Here a neutron, whose incident direction is unknown, undergoes two n-p scatters. The kinematics of non-relativistic scattering implies that the scattered neutron and proton momentum vectors will be mutually orthogonal. Since the recoil proton is not tracked due to its short range in the scintillator, a single n-p scatter does not provide sufficient information to determine the direction of the incident neutron. However, if the incident neutron undergoes at least two n-p scatters and the full energy is measured, the incident direction is restricted to the mantle of a cone whose axis is the momentum vector of the first recoil neutron. The neutron scatter direction, θ_n, is the vector between the two scatter points where

$$\sin^2 \theta_n = \frac{E_{p1}}{E_n}.$$

In general, a measure of the energy loss and interaction location at two interaction sites will not provide a measure of the full energy of the incident neutron, which can nevertheless be determined by performing a time-of-flight measurement between the first and second scatters. Alternatively, if a third interaction site can be measured, the coordinates of the third scatter provide the additional kinematic information necessary to uniquely define the incident neutron energy, albeit with an uncertainty set by the spatial and energy resolutions of the instrument.

The projection of the cone onto an image sphere results in an "event circle." The superposition of many event circles can

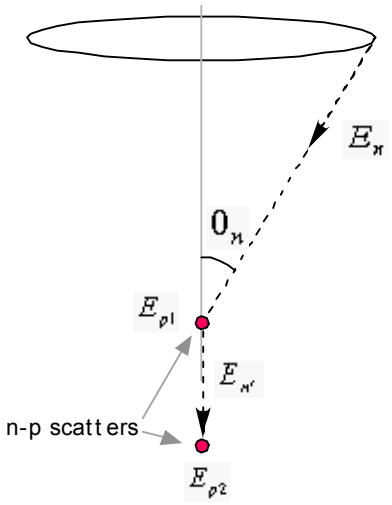

Figure 2. Double n-p scatter event. Schematic showing the basic kinematics of event reconstruction. If the full neutron energy is measured, the neutron arrival direction is restricted to lie on the mantle of a cone.

produce an image. Event circles from *e.g.* a solar flare or a localized SNM sample will intersect at some point, while unrelated (background) event circles will not. This procedure is analogous to one used successfully with the COMPTEL instrument to image MeV γ-ray and neutron sources[8].

3.2 Why an imaging detector rather than a bulk scintillator?

Bulk scintillators are efficient detectors of neutrons. Although they can be fashioned into large area instruments (such as *e.g.* SMM-GRS, OSSE and EGRET-TASC), such instruments usually provide limited information about the energy of individual neutrons. Performing the best possible measurement of the neutron energy is important because the neutron production time at the Sun is determined from the neutron energy, the measured arrival time and the distance to the Sun. Without the neutron energy information, one must assume that the neutron production follows that of the observable γ-ray emission. However, this is an *ad hoc* assumption that is often not true.

In space, neutron background is ubiquitous and intense. It is produced in all matter subject to cosmic rays. It is a problem for balloon platforms, low earth-orbiting spacecraft and spacecraft in interplanetary locations. Anywhere there are interacting cosmic rays there will be neutrons. These background neutrons generally arrive isotropically from the background emitting material that is typically distributed over large solid angles as seen from the perspective of an instrument on a payload bus. For example, the neutrons that COMPTEL measured from the June 1991 solar flares[9] were only visible because of background rejection techniques used in double-scatter instruments that were described above. Imaging neutron detectors such as COMPTEL and SONTRAC with threshold energies >20 MeV, suitable for larger heliospheric radii have been developed and in the case of COMPTEL successfully operated. However, a detector for the innermost heliosphere for neutron energies in the range 2 – 20 MeV is still missing. This gap will be filled by FNIT.

Similarly, the key to addressing the issues in SNM detection lies in the direct identification and imaging of fast fission neutrons. Specifically, neutron imaging:

- can be used to locate and measure the activity of a source; and
- permits an efficient level of background rejection that can lead to a substantial improvement in sensitivity.

One can expect that the total flux of neutrons on the detector from a ^{239}Pu source will be comparable to or less than the room background. Imaging reduces the problematic background to that coming from the approximate direction of the source—far less than the room background. Using imaging techniques, such as the ones described above, one can isolate the source signal so as to improve its significance relative to the background. Although not required for source location, a measure of the neutron energy and the reconstruction of the energy spectrum profile become extremely useful in confirming the nature of the source. Thus, FNIT is also a potential candidate instrument for SNM detection.

4. THE FAST NEUTRON IMAGING TELESCOPE

The baseline structure of FNIT, consisting of a tower of eight to ten detector layers, is shown in Figure 3. Each layer is made from a sheet of plastic scintillator. Grooves are machined into both sides of the sheet with a regular pitch and orthogonal orientations for the upper and lower surfaces. A wavelength shifting (WLS) plastic fiber is bonded into each groove and routed to one pixel on the face of a multianode photomultiplier tube (MAPMT). A small portion of the blue scintillation light created in the plastic scintillator is

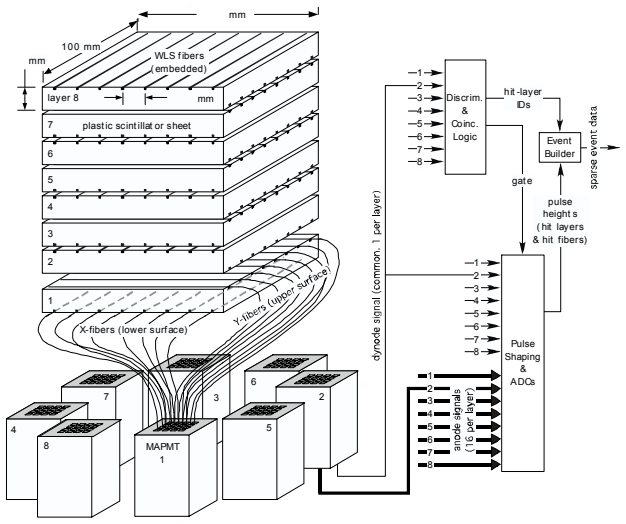

Figure 3. FNIT instrument concept utilizing WLS fiber / MAPMT readout of scintillator detector layers.

absorbed by the WLS fibers on both surfaces near the ionization location and re-emitted as green light. The clad WLS fibers act as light guides for the trapped portion of this green light signal that then travels the length of the fiber to the MAPMT pixel for readout. In this configuration one 16-anode MAPMT reads all the signals from one layer and the instrument trigger is a coincidence of signals from two or more scintillator layers. When triggered, the IDs and pulse heights of the layers and hit fibers are time-tagged and read out as event messages for further processing and analysis. Analysis of the pulse heights of the coincident signals is performed to measure the energy deposits and interaction locations. The measurement of the relative timing of signals is used to help discriminate between scattered neutrons and γ-rays. Analysis of the event data from this instrument provides the incident energy and direction of individually detected neutrons, and ultimately, for ensembles of detected events, the location and strength of the neutron source. In addition to performance requirements, an instrument for deep-space must be autonomous, efficient and low mass. Low volume, low power and combined imaging and energy measurement capabilities are crucial.

We have fabricated several prototype detector layers using plastic scintillator, WLS fibers and a 16-channel MAPMT and conducted a number of key measurements (light output, spatial, time and energy resolution). We have experimented with different plate dimensions, combined with various reflective coatings and fiber pitches, using both round and square WLS fibers. Of those tested, the best performance was achieved by the following detector layer structure:

- BC-404 plastic scintillator[10], 120 mm × 120 mm × 15 mm (thick);
- 64 evenly-spaced BCF-91A multi-clad WLS round fibers[10], diameter = 1.0 mm (32 *x*-fibers & 32 *y*-fibers);
- one Hamamatsu H8711-10, 16 channel MAPMT[11] (4×4 array);
- 4-fiber groups read out by one MAPMT anode (*i.e.* 64 fibers feeding 16 MAPMT channels);
- reflective end-mirrors.

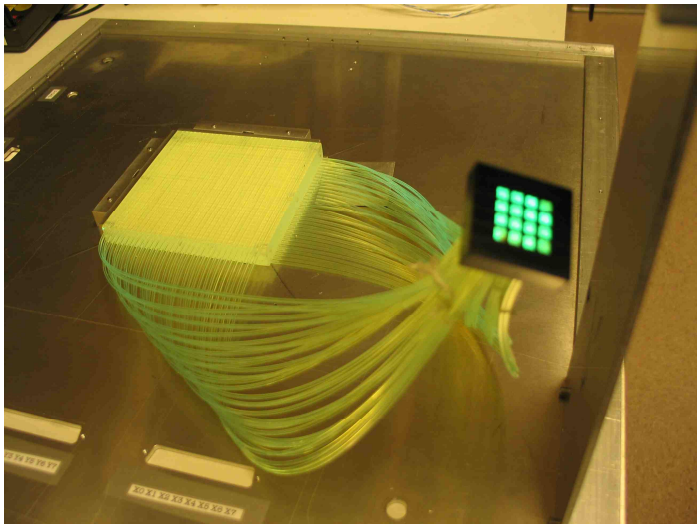

Figure 4. FNIT prototype detector layer, used in lab tests. The plastic scintillator and 64 WLS fibers are clearly visible. The black "cookie" in the foreground is coupled to the photocathode of a 16 channel MAPMT.

A photograph of this prototype scintillator layer is shown in Figure 4. The effective pitch of 4-fiber groups is approximately that of the thickness of the plate. Using 4-fiber groups rather than having a total of 16 individual fibers does not improve position sensitivity *per se*, but it increases the light yield of FNIT, which in turn lowers the energy threshold and ultimately provides better energy and position resolution.

In addition, we have also identified a promising alternative approach to the design described above. Liquid scintillators offer potential background reduction and sensitivity advantages over plastic scintillators in neutron detection applications. In addition to γ-neutron pulse shape discrimination (PSD) capabilities, liquid scintillators have higher H:C ratios and larger light outputs. At the time of writing, there are no available studies of liquid scintillators read out with WLS fibers. We are, however, encouraged to investigate the feasibility of such an alternative design by the light yield results of our present prototype and by the fact that the fast timing characteristics of available WLS materials should be sufficient to permit their effective use in PSD measurements. This has the potential of providing a significant additional background reduction mechanism for FNIT.

5. FNIT PERFORMANCE

5.1 Simulations

A Monte Carlo simulation code based on the GEANT4[12] package has been developed to support the FNIT design effort. It is now being used to optimize the configuration of FNIT, determine its overall efficiency, develop and test analysis

software for incident particles and estimate count rates for both solar neutrons and background events. The sensitivity of a FNIT tower consisting of 10 scintillator layers, 100 mm × 100 mm × 15 mm in size, obtained with this code assuming vertically-incident neutrons, is shown in Figure 5. Peak efficiencies of up to 50% (including over 10% for double/triple scatter events) are achieved at a few MeV and neutrons can be detected, albeit with decreased performance, to energies of over 100 MeV. While FNIT is being developed primarily for neutrons with E_{kin} < 20 MeV and a dedicated detector such as *e.g.* SONTRAC is better suited for higher energies, this extended range provides critical cross-calibration capability.

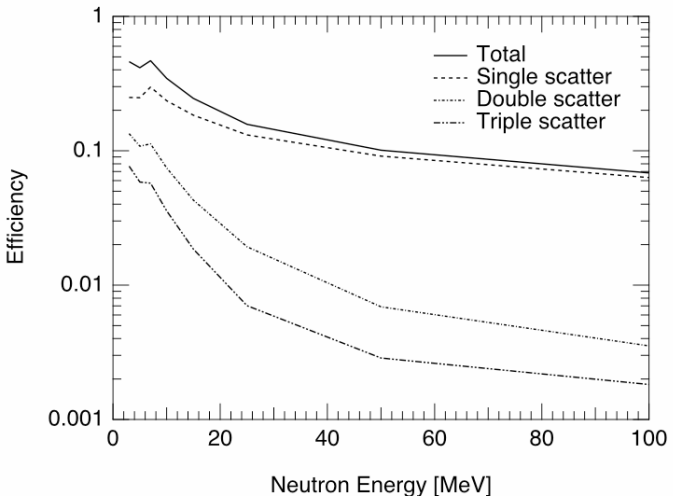

Figure 5. FNIT detector efficiency for single, double and triple n-p scatters, determined with Monte Carlo simulations.

We also estimated the solar neutron count rates for this FNIT tower, assuming a 0.3 AU solar orbit and a fixed effective area (*i.e.* the FNIT detector pointing at the Sun at all times). We simulated the 30-minute neutron signal after the onset of the X12 class solar flare of 15 June 1991[13]. Our results for this scenario show that FNIT would detect approximately 1700 double elastic n-p scatters in the energy range 3-10 MeV from a flare of this class. Estimating background neutrons is more difficult. For that we used an isotropized atmospheric albedo spectrum to represent the flux from a thick low-Z target and estimated about 100 background neutron counts in the range 3-10 MeV. Thus, our signal to noise ratio should allow for the clear identification of solar flare neutrons, although we did not include the backgrounds from γ-rays and charged particles in our simulations at this time. These results illustrate the importance of Monte Carlo tools for the design optimization effort, as well as the present level of maturity of our simulation software.

5.2 Testing setup

As mentioned in the previous section, we have built a small number of FNIT scintillator layer prototypes with different designs and determined the main physics parameters of each layer individually. The main differences among these prototypes were in the layer dimensions and type of scintillator material, number of fibers and fiber pitch. We also compared round vs. square fibers, attempted to minimize the distance between the scintillator and the photocathode to reduce attenuation losses in fibers and experimented with different reflective coatings and end-mirrors on the scintillator layers. We used a 16-channel MAPMT to read out the WLS fibers. In addition to the anode signals, we also recorded a dynode signal from this MAPMT, which all fibers contributed to. The FNIT scintillator layer was augmented by a plain plastic scintillator (auxiliary detector), placed on top of FNIT at a distance of 30 cm, used for trigger in coincidence with the MAPMT dynode and time of flight (TOF) measurements. The readout electronics were installed in a standard CAMAC crate and the KMAX 7.4.2[14] software was used for data acquisition (DAQ). Results presented in the following paragraphs are for the best-performing detector prototype configuration described in Section 4.

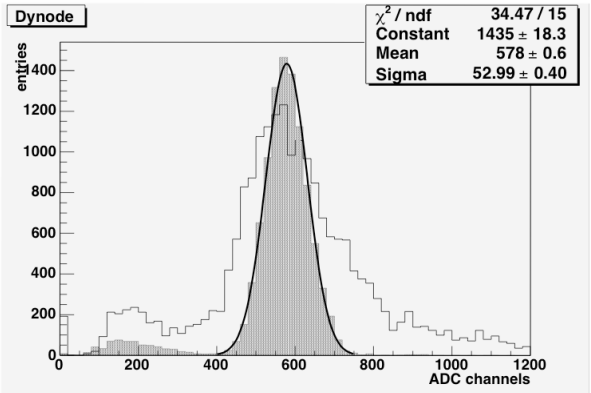

Figure 6. ADC distributions from FNIT dynode. Muon peak (blank) and LED peak (shaded with Gaussian fit), used to determine FNIT $\delta E/E$ and light yield.

5.3 Light yield, energy and time resolution

To determine the light yield of the FNIT prototype, we first acquired a sample of dynode signals produced by ground level cosmic-ray muons. We used our Monte

Carlo code to determine that the muon peak in Figure 6, produced by minimum ionizing particles, corresponds to an energy of 2.63 MeV. We then installed a green-light LED in front of the photocathode and varied its intensity to generate a signal overlapping the muon peak. From the values of the mean and the σ of the LED peak, driven primarily by Poisson statistics, and the energy scale determined by the muon peak, we calculated that our FNIT prototype provides a light yield of 41 photoelectrons / MeV (electron equivalent).

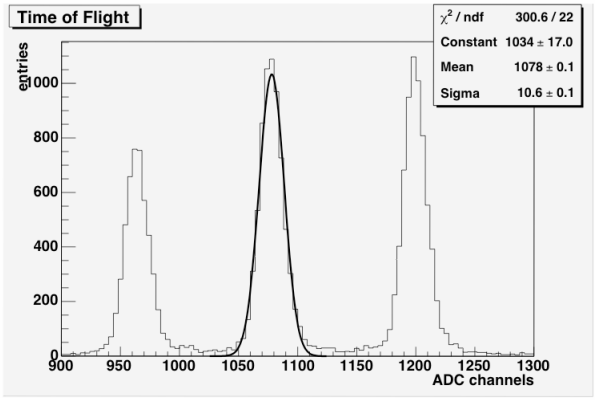

Figure 7. Time of flight measurements. The gaps between adjacent peaks correspond to a 7 ns delay.

The energy resolution was determined again from the distributions in Figure 6. Specifically, we fitted the upslope of the muon peak with a Gaussian. This distribution being the convolution of the Landau *dE/dx* energy loss fluctuations[15] and the Gaussian energy resolution function, we then subtracted in quadrature the σ-component from Landau fluctuations, estimated again with the Monte Carlo code. The remaining σ-value was used to determine the energy resolution figure. We found that at 2.63 MeV the 1 σ resolution is $\delta E/E \approx 17\%$, to be compared to the Poisson-statistics limit on energy resolution at this energy, which is approximately 10%.

Finally, time resolution was determined by measuring the time of flight of cosmic-ray muons between the auxiliary detector and the FNIT scintillator layer. We used delay lines of 0, 7 and 14 ns between the START and the STOP signals of the TOF modules (which consisted of a TAC and ADC) and did no selection/analysis on the muon events (*i.e.* we assumed that all cosmic-ray muons had the same time of flight). Figure 7 shows the three peaks from these three delay lines. From the σ-values of the Gaussian fits and the absolute scale determined from the peak values, we estimated a 1 σ upper limit on the time resolution of $\delta t = 0.6$ ns, to be compared to the TOF between the auxiliary detector and the FNIT module in our setup (30 cm distance), which is ~1 ns for a γ-ray and ~7 ns for a 10 MeV neutron. In the case of the full FNIT configuration shown in Figure 3, TOFs between layers will vary from ~0.1 ns to ~1 ns for γ-rays (and scale similarly for neutrons), depending on the position of the two layers where the interactions occur, while the δt should be comparable to our measured value. Therefore, in most cases we expect to be able to separate slow 10 MeV double-scatter neutrons from Compton-scatter events induced by γ-rays, as well as from upgoing albedo neutrons produced from interactions in the spacecraft, by using TOF measurements alone.

5.4 Position resolution

Position resolution was determined by exposing the FNIT prototype layer to a collimated ^{90}Sr β-source, emitting electrons with $E_{max} = 2.28$ MeV. We used the MAPMT anode signals to reconstruct the position along the two horizontal axes and experimented with different analysis algorithms to determine the *x* and *y*-coordinates from the signals recorded by the 16 anode channels. Specifically, we compared the resolutions achieved along each cartesian axis by deriving the position from the:

- MAPMT anode with the largest signal;
- σ of the Gaussian fit and/or weighted mean of the three neighboring MAPMT anodes with the largest signals; and
- σ of the Gaussian fit / weighted mean ("center of gravity") of all eight anodes along one axis[16].

Best results, shown in Figures 8 and 9, were obtained by the Gaussian fit to the three largest adjacent signals. For a β-source located in the center of the FNIT layer, we obtained a 1

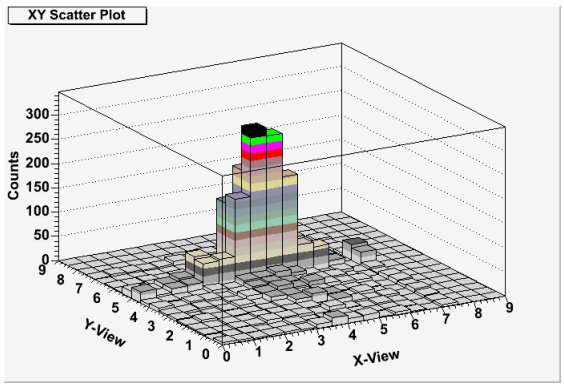

Figure 8. FNIT horizontal position resolution; *x*-*y* scatter-plot of the peak produced by a ^{90}Sr source. The scales on the *x* & *y* axes in Figures 8-10 are "MAPMT anode pitches" (see text): one unit increment corresponds to an individual 4-fiber group.

σ resolution of δy = 0.30 MAPMT anode pitches = 4.5 mm along the *y*-axis and δx = 0.83 MAPMT pitches = 12.5 mm along the *x*-axis. This difference in resolution is due to the fact that ^{90}Sr β-electrons have a limited range of < 10 mm in the FNIT scintillator, combined with the effects of multiple scattering on the β-particle's trajectory. Therefore, the light signal collected by *y*-fibers, bonded in the grooves on the top-side (irradiated side) of the scintillator layer, is more localized than the signal measured by the *x*-fibers on the bottom side.

These results were obtained with the scintillator layer configuration described in Section 4, where 4-fiber groups were connected to one MAPMT anode channel, (*i.e.* each horizontal coordinate consisted of 32 fibers that were read out by 8 anodes). Because of this, resolutions are quoted in "MAPMT anode pitch" units. When compared to scintillator layers with 8 fibers per coordinate feeding 8 anodes, 4-fiber groups provided a better position resolution. This was not due to a smaller fiber pitch, since resolution was limited by the horizontal sampling frequency of the anode channels, which remained unchanged. Rather, 4-fiber groups provided a 20-30% better light yield, which improved the performance of our position reconstruction algorithm and ultimately led to a better position resolution.

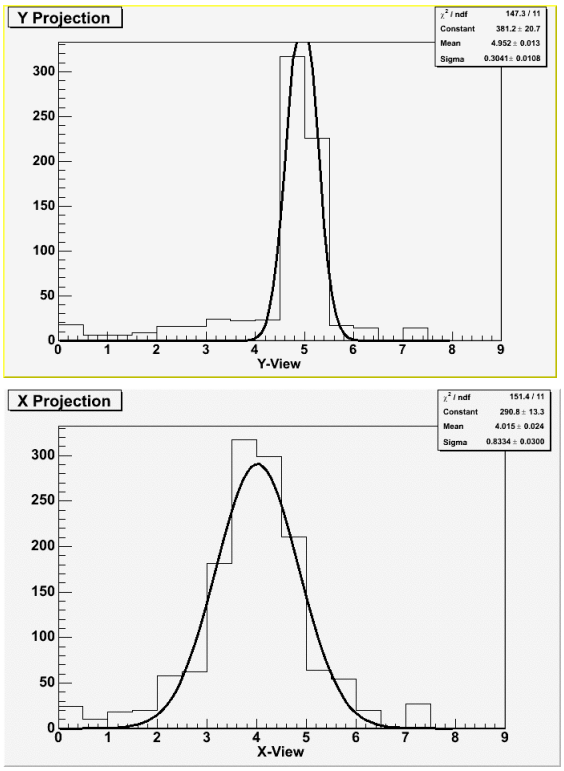

Figure 9. Projections of the plot shown in Figure 8 along the two horizontal axes. The peak is significantly narrower along the irradiated *y*-fibers.

We also checked the dependence of these δx and δy figures on the *(x,y)* position of the ^{90}Sr source on the FNIT scintillator layer. Moving the β-source from the center towards the edges of FNIT slightly deteriorated the resolution figures quoted above, but our position reconstruction algorithm proved to be sufficiently robust, except for cases where the ^{90}Sr source was positioned next to the extremity of the scintillator layer. To check for any systematic errors introduced in the reconstruction process, we also compared the difference between the reconstructed and actual position of the ^{90}Sr source on the FNIT layer as a function of the actual position. Results are displayed in Figure 10 and demonstrate the level of maturity achieved by our analysis software.

5.5 Energy threshold

After analyzing cosmic-ray muons and the ^{90}Sr electrons, we also studied the signal from lower energy sources: ^{57}Co, ^{60}Co, ^{133}Ba, ^{137}Cs and ^{241}Am. For each source, we determined the horizontal position resolution and identified a signal feature in the MAPMT dynode distribution (Compton edge in the case of γ-sources). As an example, Figure 11 shows the ADC distribution from the ^{60}Co γ-source. The Compton edge, with a nominal energy $E_{Compton} \approx 1$ MeV, can be clearly identified and separated from the pedestal peak.

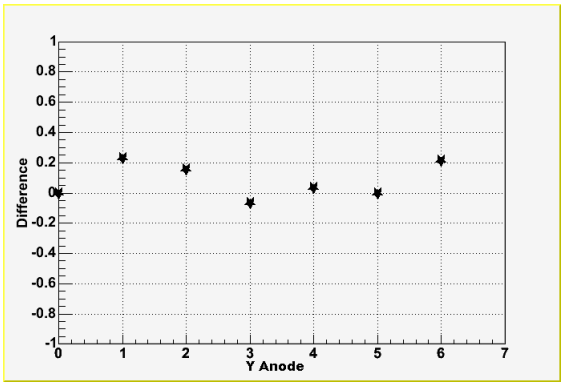

Figure 10. Quality check for the position reconstruction algorithm. Difference between the actual position and reconstructed mean value of the position of a ^{90}Sr source as a function of the actual position.

We estimated the energy threshold of the FNIT prototype layer to be 250 keV (electron equivalent), which corresponds to a light yield of ~10 photoelectrons. At this energy, which falls between *e.g.* the ^{57}Co and ^{137}Cs sources, the Compton edge is barely visible and the position resolution is $\delta x \approx 100$ mm. We were still able to visually identify features in the

dynode spectrum and in the *x*-*y* scatterplots from sources below this threshold, such as ^{241}Am, but they were not statistically significant and hardly of any use in a quantitative analysis.

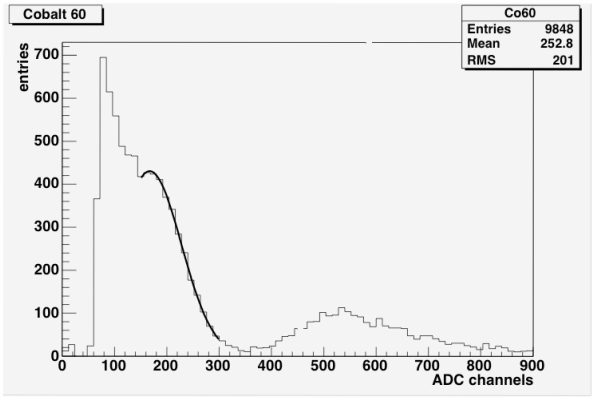

Figure 11. Dynode ADC distribution showing the muon peak (around channel 550) and the Compton edge produced by the ^{60}Co γ-source (with fitted Gaussian slope).

5.6 Summary

BC-404[10] was identified as the best choice for plastic scintillator. Our tests showed virtually no difference in performance between round and square fibers. Reducing the distance between the scintillator and the MAPMT photocathode to minimize light attenuation produced a barely measurable effect: the attenuation length for all types of fibers used in FNIT prototypes was 3 m or more, while the scintillator-MAPMT gap was varied by less than 50 cm.

A conclusion that emerged from our tests is that light yield is the crucial parameter that drives both energy and position resolution. Therefore, both of these resolutions improved when we introduced the 4-fiber groups per anode channel, which increased the light yield by as much as 20-30%. Using reflective mirrors to terminate the fibers at the extremity opposite the photocathode also had a measurable effect on light output and overall performance. Finally, we experimented with diffuse reflective coating and mirror-like coating of the scintillator layer. While light yield did not vary significantly among these two cases, position resolution was measurably better in the latter by 10-20%, due to the fact that light pulses were more localized.

6. CONCLUSIONS AND FUTURE WORK

Our goal is to develop and demonstrate a mature design for a compact, efficient, high performance neutron detector for imaging and spectroscopy in the 2 to 20 MeV energy range, suitable for use in space to measure solar neutrons, which can also be used in commercial and security applications.

We have developed Monte Carlo simulation tools based on the GEANT4 package and validated these tools for spectroscopic and multi-hit response. Additional simulation work is needed to fully model the inner heliosphere background of FNIT, determine its performance in SNM search applications and select the optimum structure of the full FNIT multi-layer tower. Finally, we plan on upgrading our present analysis software for multi-hit events.

A number of individual prototype FNIT scintillator layers were engineered and tested. We identified the configuration that provides the best performance and froze the one-layer design. At present, we are investigating alternatives to the baseline FNIT configuration, *e.g.* the use of liquid scintillators. We are also in the process of upgrading our DAQ hardware and migrating from CAMAC to a VME system. Finally, our near term plans include the building and testing of a tower consisting initially of three FNIT scintillator layers and its exposure to a neutron source, to evaluate the actual performance of FNIT in neutron detection.

ACKNOWLEDGMENTS

We would like to acknowledge the financial support for the FNIT project by our funding agencies: NASA (grant NAG5-13519) and the DoE (contract DE-FG52-04NA25687) in the United States and the Swiss National Science Foundation (grant 200020-105435/1) in Switzerland.

REFERENCES

1. J.A. Lockwood, H. Debrunner, and J.M. Ryan, "The Relationship Between Solar Flare Gamma-Ray Emission and Neutron Production", *Solar Phys.*, vol. 173, pp. 151-176, 1997.

2. http://lws.gsfc.nasa.gov/missions/sentinels/sentinels.htm
3. M.R. Moser, E.O. Flückiger, J.M. Ryan, J.R. Macri, and M.L. McConnell, "A Fast Neutron Imaging Telescope for Inner Heliosphere Missions", *Adv. Space Res.,* doi:10.1016/j.asr.2005.03.037, 2005 (in press).
4. R.S. Miller, J.R. Macri, M.L. McConnell, J.M. Ryan, E. Flückiger, and L. Desorgher, "SONTRAC: An imaging spectrometer for MeV neutrons", *NIM*, vol. A505, pp. 36-40, 2003.
5. J.M. Ryan, J.A. Lockwood, and H. Debrunner, "Solar Energetic Particles", *Space Sci. Rev.*, vol. 93, pp. 35-53, 2000.
6. J.M. Ryan, "Long Duration Solar Gamma-Ray Flares", *Space Sci. Rev.*, vol. 93, pp. 581-610, 2000.
7. http://cossc.gsfc.nasa.gov
8. J.M. Ryan, et al., "COMPTEL as a Solar Gamma Ray and Neutron Detector", in *Data Analysis in Astronomy IV*, Ed. V. Di Gesù, et al., Plenum Press, NY, pp. 261-270, 1992.
9. H. Debrunner, J.A. Lockwood, J.M. Ryan, M.L. McConnell, V. Schönfelder, H. Aarts, K. Bennett, and C. Winkler, "Neutrons fron the 15 June 1991 Solar Flare", *Proc. 23rd Int. Cosmic Ray Conf.*, vol. 3, pp. 115-118, 1993.
10. http://www.photonic.saint-gobain.com
11. http://www.hamamatsu.com
12. S. Agostinelli, et al., "GEANT4: A Simulation Toolkit", *NIM*, vol. A506, pp. 250-303, 2003.
13. L. Kocharov, H. Debrunner, G. Kovaltsov, J. Lockwood, M. McConnell, P. Nieminen, G. Rank, J. Ryan, and V. Schönfelder, "Deduced spectrum of interacting protons accelerated after the impulsive phase of the 15 June 1991 solar flare", *Astron. Astrophys.,* vol. 340, pp. 257-264, 1998.
14. http://www.sparrowcorp.com
15. L.D. Landau, *J. Exp. Phys. (USSR),* vol. 8, pp. 201-210, 1944.
16. G. Landi, "Properties of the center of gravity as an algorithm for position measurements", *NIM*, vol. A485, pp. 698-719, 2002.